

## Modelling of the temperature distribution of spot-weldable composite/metal joints

Sven Roth, Jonas Nieschlag<sup>\*</sup>, Malte Mehner, Sven Coutandin, Jürgen Fleischer

wbk Institute of Production Science, Karlsruhe Institute of Technology (KIT), Kaiserstr. 12, 76131 Karlsruhe, Germany

### ARTICLE INFO

#### Keywords:

Composite/metal joints  
Resistance spot welding  
Temperature distribution  
Fibre-friendly hole making

### ABSTRACT

Resistance spot welding is the most economical joining method for the production of automotive steel bodies. In modern car body construction, however, its future applicability is limited due to the growing mix of materials in multi-material design. In response to increasing weight reduction requirements to protect the environment and natural resources, lightweight materials, and fibre-reinforced plastics (FRP) in particular, are more and more used in modern vehicle bodies. To facilitate the future joining of FRP/steel structures with resistance spot welding, spot-weldable force-introduction elements may be embedded in the laminate as a joining interface. When welding the so-called inserts, thermal damage to the surrounding polymer should be avoided, as this is the only way to calculate the strength of the joint correctly. For this purpose, the paper presents a numerical model that allows the prediction of the temperature propagation during spot welding of FRP/steel joints with embedded inserts. The simulative approach is subsequently validated by comparison with experimentally determined temperature curves and in doing so, an excellent model prediction can be noted.

### Introduction

Continuous fibre-reinforced plastics (FRP) are predestined for realising the lightest possible load-bearing structures with high component stiffnesses and strengths (Fleischer et al., 2018) such as those required in lightweight automotive body construction (Njuguna, 2016). An economically viable implementation in large-scale production can be achieved by a targeted combination of metal components in the so-called multi-material design (Roquette et al., 2017). In this approach, each component's material is selected according to the prevailing component requirements.

In practical applications, FRP have so far mainly been joined to metallic body components by adhesive or mechanical joining methods (Fleischer et al., 2018). In contrast to resistance spot welding, which is considered to be the preferred joining technique for steel-intensive constructions (Pischinger and Seiffert, 2016), they involve significantly higher development and equipment costs. In case of modern adhesives, the curing time limits the achievable cycle time in production and complicates the implementation in large-scale production (Friedrich, 2017). The use of additional elements that penetrate the component, however, leads to structural damage of the fibre composite, which results in the weakening of the joint (Fleischer et al., 2018). The

cutting of the load-bearing fibre structure causes the strength of the joint to decrease and the lightweight potential remains unexploited (Lin and Lee, 1992).

A promising approach to an economic implementation of the multi-material design in large-scale production is therefore the joining of FRP and metal components by means of resistance spot welding (Roth et al., 2019). Metallic load introduction elements inserted in the fibre composite serve as the joining interface for the welding process (Boutaris et al., 2011). The insertion of the load introduction elements takes place during the component production of thermoplastic (von Hehl et al., 2016; Kunze et al., 2016) as well as of duroplastic (Roth et al., 2019; Roth et al., 2020c; Ruffing and Baron, 2019; Weatherhead, 1980) composite parts. For the latter, the RTM process in particular shows great potential for industrialisation in large-scale production (Njuguna, 2016). It enables fibre-friendly hole making for embedding the load introduction elements already during preforming, and the individual rovings of the textile semi-finished product are reoriented around the joining area and not destroyed. This leads to an increase in load-bearing capacity of the infiltrated component by 25% due to better material utilisation (Gebhardt et al., 2018).

During resistance spot welding of steels and sheet thicknesses commonly used in body construction, the use of spot-weldable force

<sup>\*</sup> Corresponding author.

E-mail address: [jonas.nieschlag@kit.edu](mailto:jonas.nieschlag@kit.edu) (J. Nieschlag).

introduction elements results in a heat-affected zone in the area close to the welding point (Roth et al., 2020c). Within this zone, temperatures above the decomposition temperature of common epoxy resins are reached (Visakh and Visakh, 2015; Natarajan and Murugavel, 2017). If the joint is incorrectly designed, it will cause irreversible damage to the FRP due to physical and chemical ageing processes of the matrix. These are manifested by a change in the molecular structure and the polymer texture, leading to a reduction of the mechanical properties to an unknown extent (Domininghaus et al., 2012).

### State of the art and preliminary work

In order to avoid thermal damage to the laminate during spot welding, precise knowledge of the temperature distribution in the joining area during spot welding is required. There are already extensive studies dealing with the description of the temperature field during spot welding of pure metal joints (Akkus, 2009; Cho and Cho, 1989; Han et al., 1989; Lee et al., 2017; Lu et al., 2018; Nied, 1984; Wan et al., 2014; Wang et al., 2015; Zhao et al., 2019). According to these studies, the heat transfer, the amount of heat introduced to form the welding lens as well as the geometry and material characteristics of the electrodes and joining partners in contact have a significant influence on the temperature distribution (Radaj, 1988). In the context of force introduction elements not embedded in the FRP, these influencing variables have already been investigated experimentally (Roth et al., 2020c). However, the numerical approach for transferring the findings to different welding parameters, material pairings or electrode geometries lacks these experimental investigations. The temperature distribution in the embedded state is not known either. A dimensioning of the joint while avoiding thermal degradation of the matrix during spot welding is thus not possible.

To counter this shortfall, it is necessary to consider the thermal properties of the fibre composite in the joining area. Due to the anisotropic fibre properties and locally different fibre volume contents, reorienting the fibres when embedding the load introduction elements leads to a different material behaviour compared to the undisturbed laminate (Hartmann et al., 2020). A description of the fibre paths as they arise during the fibre-appropriate embedding process is based on two fundamentally different approaches in the current state of research.

On the one hand, substitute models can be used, which show the fibre path in a highly simplified way, for example through its similarity to streamlines (Lin and Lee, 1992; Lin and Yang, 1993; Lin et al., 1995; Ng et al., 2001; Hartmann and Kheiri Marghzar, 2018; Ghasemi Nejjhad and Chou, 1990). However, these models do not take into account any influences from the textile behaviour or the hole forming process and are therefore not suitable for a precise description of the reoriented fibres. On the other hand, descriptive approaches exist which allow a prediction of the fibre paths taking into account material and process variables. The majority of them is limited to the hole-making in fibre-reinforced thermoplastics (Leiser, 2006; Hufenbach et al., 2011; Kupfer, 2016). It is not possible to transfer this method to hole forming in textile semi-finished products. This deficit is addressed by (Roth et al., 2020a) with the help of an analytical approach, which allows a description of the fibre paths in textile semi-finished products taking into account material and process properties. Its use enables accurate prediction of the thermal properties of the fibre compound in the joining area of spot-weldable FRP/metal parts.

The aim of this paper is to model the temperature distribution during spot welding of FRP/metal joints, taking into account the fibre paths as a result of a fibre-friendly integration of the load introduction elements. For this purpose, a modular, numerical approach is used. It ensures a damage-free design of the joint and thus a cycle time-optimised joining of FRP/metal joints in car body construction.

### Numerical modelling

The developed finite element model can be grouped into three parts, which are presented below. As a first step, the geometry data of the considered joint – consisting of FRP, insert and joining partners – is parameterised and entered using the finite element software COMSOL Multiphysics 5.4. This is followed by a partitioning into several individual cells to map the anisotropic material properties of the laminate after the fibre-friendly hole forming. As a second step, the material properties are assigned to these cells in a discretised manner, whereas the local fibre volume content can be taken into account according to the fibre path with the approach of Roth et al. (2020a). In addition to the description of the fibre composite, the characteristic values of all other materials are assigned. In the third step, the welding heat is modelled on the basis of Joule heating by using the process variables welding time and welding current as input variables.

#### Geometric model structure

To investigate the temperature curve and in particular the temperature maxima, taking into account the local fibre orientations of the FRPs, the specimen shown in Fig. 1 was investigated using the finite element method. The basic arrangement of metallic insert and fibre composite is based on applications in practice (Ruffing and Baron, 2019). The specimen dimensions are chosen in accordance with (Roth et al., 2020c), where the diameter of the opening in the laminate  $\varnothing_{hole}$  is kept variable (see Fig. 1 on the right).

The value for the outer dimension of the laminate is derived from the research results of Wan et al. (2014). With an additional safety factor, the sample width is dimensioned at 50 mm, so that an influence of a small sample size on the temperature propagation can be excluded. Fig. 2 shows the setup including the welding electrodes, type ISO-G0-16-20-40-6-15 according to DIN EN ISO 5821, that need to contact the insert on both sides to carry out spot welding. Due to the symmetry in the fibre path of the considered biaxial fabric (Roth et al., 2020a), a quarter model is simulated to save computing time (see Fig. 2 on the right).

#### Model assumptions

The aim of finite element welding process modelling with the software COMSOL is to calculate the heat propagation in the insert and the laminate. For this reason, some physical assumptions and simplifications have to be made for the modelling.

No force influences are considered as the influence on the heat distribution is classified as insignificant. Thus, no electrode marks are modelled on the sheets to be welded, and the contact resistance is independent of the electrode contact pressure. Deformation and dynamic electrode contact resistance are assumed to have neglectable impact on the thermal behaviour and temperature development in a distance to the nugget on the insert and the CFRP close by. For the modelling of the electric current, it is assumed for simplification that the current only flows through the metallic components of the model: welding sheets and electrodes (see Fig. 2– light grey) since the electric current always takes the lowest resistance. In addition, the interface layer between insert and CFRP consists of a matrix layer and is not electrically conductive.

In addition, the contact resistance between the welding partners is defined as a constant. Contact resistances between the electrodes and the steel sheets are minor and thus neglected.

All materials defined in the model have the temperature-dependant properties: specific heat capacity and specific thermal conductivity. The temperature-dependant specific electrical conductivity is implemented as well, for the electrode material and the steel. In addition, two further simplifications are made for the steel components: The dislocation accumulation which arises as a result of deep drawing to the insert geometry is not mapped, and the phase transformations in steels are not

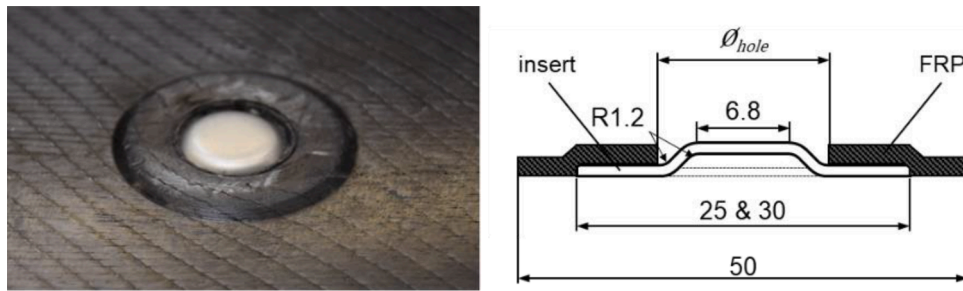


Fig. 1. Specimen overview of the spot-weldable composite/metal joint with variable diameter of the opening in the laminate  $\varnothing_{hole}$ .

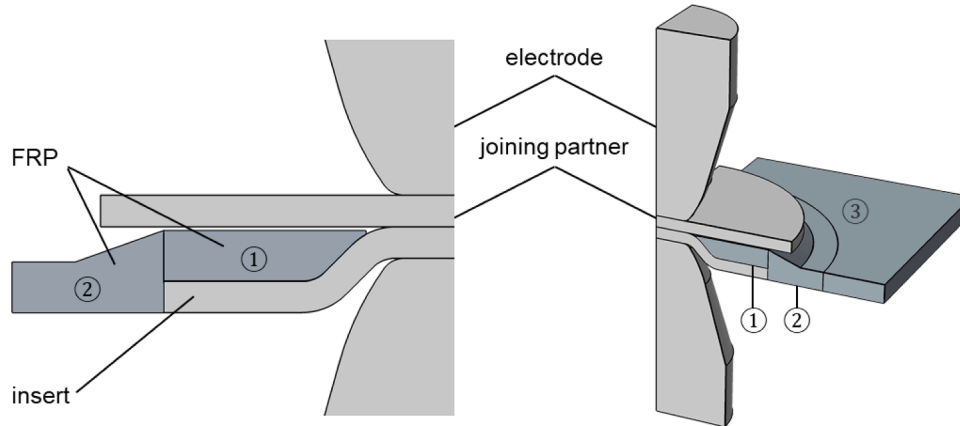


Fig. 2. Model geometry in COMSOL Multiphysics.

considered. The carbon fibre reinforced plastic (CFRP) is mapped using effective material parameters (Table 1). These parameters take the local fibre volume content and fibre orientation into account. A macroscopic homogenisation of the microscopically inhomogeneous composite material takes place. Therefore, no internal thermal barriers between fibre and matrix as well as between individual fibre layers are modelled in the CFRP section of the model. Finally, the fibre layers are combined in a  $0^\circ$  or  $90^\circ$  orientation. The fibre orientation is mirrored between the central layers.

### Material properties

The calculation of the specific thermal conductivity and heat capacity of the CFRP is based on a mathematical 2D model based on cubic splines, which describes the path of the carbon fibres around the hole of the CFRP component (Roth et al., 2020a). For calculation purposes, the CFRP area is divided into individual small partitions with a square base and the layer thickness as height (see Fig. 3). The material properties within a partition are homogenous. The directional properties are dependant on the angle between the fibre and the temperature gradient as well as on the local fibre volume content (Tables 1 and 2). The latter can be determined on the basis of Roth et al. (2020a) and the calculated fibre volume content in the undisturbed laminate.

The material parameters were calculated and provided for the COMSOL simulation programme using a Matlab script. Parallel to the fibres, the mixing rule according to Voigt (1889) applies:

$c_{Voigt}(T) = v_F \cdot c_{F, parallel} + (1 - v_F) \cdot c_M(T)$ , and perpendicular to it, the Reuss model (Reuss, 1929) offers an approximation:

$$c_{Reuss}(T) = \left[ \frac{1}{v_F \cdot c_{F, quer}} + \frac{1}{(1 - v_F) \cdot c_M(T)} \right]^{-1}$$

A weighting of the two amounts is performed depending on the actual angle  $\gamma$  with the addition theorem (Pilling et al., 1979):

$$c_{eff}(T) = c_{F, Voigt}(T) \cdot \cos^2 \gamma + c_{F, Reuss}(T) \cdot \sin^2 \gamma,$$

with

- $v_F$  = fibre volume ratio of the component
- $c_{Voigt}(T)$  = effective thermal conductivity of a composite according to the Voigt model
- $c_{Reuss}(T)$  = effective thermal conductivity of a composite according to the Reuss model
- $c_{F, parallel}$  = effective thermal conductivity of the fibre in fibre direction
- $c_{F, quer}$  = effective thermal conductivity of the fibre transverse to the fibre direction
- $c_M(T)$  = thermal conductivity of the matrix depending on the temperature in K

The heat capacity is calculated with the mixing rule according to Voigt, as it is independent of direction. The local fibre volume content can be derived from the distance between two fibre strands. The value is flexible between the fibre volume content in the undisturbed laminate (minimum) and in the immediate vicinity of the hole (maximum). The local maximum fibre volume content was determined on the basis of microscope images and amounts to 72% in the present application. Calculated results are provided as a temperature-dependant term for the simulation program.

The material parameters - thermal conductivity and heat capacity - of the epoxy resin and the steel were determined on the basis of own measurements using a dynamic differential calorimeter (NETZSCH DSC 204). The temperature-dependant material properties of the individual materials are listed in Tables 1 and 2. The thermal contact resistances of steel and CFRP (Gibbins, 2006), which promise good comparability for the given material pairing, are also taken from the literature.

**Table 1**  
Specific temperature-independent material parameters.

	Fixed model parameters	Value	Source
$\rho_f$	Density of the fibre	1.80 g/cc	(Toray Composite Materials America, Inc. T700S 2020)
$\rho_m$	Density of matrix	1.15 g/cc	(Sika Deutschland, 2021)
$\rho_F$	Density of the fibre composite	1.44 g/cc	Calculated
$\rho_i$	Density of the insert	7.86 g/cc	(Richter, 2020)
$\rho_S$	Density of the joining sheet	7.86 g/cc	(Richter, 2020)
$\rho_E$	Density of the welding electrode	8.91 g/cc	(Deutsches Kupferinstitut 2021)
$\epsilon_{m, \text{matrix}}$	Emissivity of the matrix	0.96	(SIKA Dr. Siebert, and Kuhn GmbH, and Co. KG 2020)
$\epsilon_{m, \text{insert}}$	Emissivity of the insert	0.75	(SIKA Dr. Siebert, and Kuhn GmbH, and Co. KG 2020)
$\epsilon_{m, \text{sheet}}$	Emissivity of the joining sheet	0.75	(SIKA Dr. Siebert, and Kuhn GmbH, and Co. KG 2020)
$\epsilon_{m, \text{el}}$	Emissivity of the welding electrode	0.07	(SIKA Dr. Siebert, and Kuhn GmbH, and Co. KG 2020)
$c_{p, f}$	Specific heat capacity of the fibre	753.60 J/(kg K)	(Toray Composite Materials America, Inc. T700S 2020)
$\lambda_{f  }$	Thermal conductivity of the fibre in longitudinal direction	9.40 W/(m K)	(Toray Composite Materials America, Inc. T700S 2020)
$\lambda_{f\perp}$	Thermal conductivity of the fibre in the transverse direction	0.94 W/(m K)	(Toray Composite Materials America, Inc. T700S 2020)
$V_{f,0}$	Fibre volume content in the undisturbed laminate	0.44	Calculated
$V_{f, \text{max}}$	Maximum fibre volume content in the undisturbed laminate	0.72	Measured
$h_{EF}$	Therm. contact conductivity: Interface electrode - joining sheet	250 kW/(m <sup>2</sup> K)	(Bardon and Tahar, 2001)
$\lambda_{ws}$	Resistance layer conductivity: Interface insert - fibre composite	0.47 W/(m K)	Estimated
$d_{ws}d_{ws}$	Resistance layer thickness: Interface insert - fibre composite	23 $\mu\text{m}$	Thickness of matrix
$R_{FF}$	Surface impedance: Interface insert - fibre composite	$5.655 \cdot 10^{-11} \Omega\text{m}^2$	Fitted from measurement
<b>Function-defined parameters f(T)</b>			
$\lambda_{Ep}$	Thermal conductivity of the epoxy matrix	$0.158 \cdot \exp(0,003,234 \cdot T)$	Fitted from measurement
$c_{Ep}$	Heat capacity of the epoxy matrix	$528.3 \cdot \exp(0,0,009,132 \cdot T)$	Fitted from measurement

### Simulation results

The simulation focused in particular on the heat propagation behaviour in radial direction, especially in the area of the CFRP. The results were calculated with a free mesh with edge lengths between 0.05 mm and 0.3 mm obtained from the convergence analysis. The welding time of 300 ms and the subsequent cooling time up to a total duration of 2 s were simulated.

As Fig. 4 exemplifies for  $\phi_{hole} = 9$  mm, the maximum heat propagation appears after 0.90 s on the underside of the insert (1). The temperature progresses faster in the steel than in the CFRP, resulting in a vertical temperature gradient in the CFRP, with the warmer area at the bottom where the insert is located (2). After 1.24 s, an almost vertical course of the 149 °C isotherm has set in between the individual CFRP

layers (3). With increasing cooling, it becomes apparent that the area with the highest temperature lies in the area close to the insert. Based on the 149 °C isotherm, it can be observed from 1.56 s onwards (4). This warm ring-shaped area has a width of 0.4 mm. After 1.60 s, the temperature in the entire model is again below 149 °C. In the area of the heat ring, the temperature is above 149 °C for almost one second.

The investigated influencing factors: CFRP hole diameter, insert diameter, energy input have different influences. While the insert diameter can be classified as almost irrelevant for the radial temperature propagation, the hole diameter  $\phi_{hole}$  does have a significant influence. By increasing this diameter, the temperature advances further in the radial direction. This is due to the lack of material and thus the overall lower heat capacity in this area of the sample. The influence of the welding current, which is representative for the energy input at this point, is twice as great.

A sensitivity analysis was carried out on the most important model parameters: contact resistance between the welding partners as well as the electrical and thermal conductivity of the used steel and its heat capacity. The sensitivity analysis was carried out because there were different values in literature, especially for higher temperatures. In the range above 700 °C, the parameter was reduced or increased by 30% in each case. The results for the significant factors are listed in Table 3. The analysis shows that the electric contact resistance as well as the electrical conductivity of the insert significantly influence the temperature propagation in the outer area where the CFRP has been placed. The effect of thermal conductivity variation and heat capacity variation is insignificantly small and therefore not presented in the form of a table.

The fibre orientation has no significant influence on the thermal conductivity of the CFRP in the area directly around the insert. By guiding them around the insert, the fibres at the insert lie transversely to the temperature propagation gradient, independent of the fibre orientation of the individual layer. As a result, the fibres are not capable of dissipating the heat well away from the insert.

### Experimental investigation and comparison with numerical modelling

Experimental tests are carried out to determine the quality of the numerical model. The local maximum temperatures in the CFRP are identified in welding tests with the aim of determining the temperature differences between the numerical model and the experiment. The deviation of the numerical model from the experiment can be qualified on the basis of these differences.

The given insert geometries from Section 3 are used for the comparison. The welding parameters are also chosen in accordance with the numerical model and are 8.5 kA for 0.3 s. These welding parameters are right below the critical values where splatters occur according to previous tests and the material specific surface area diagram (Roth et al., 2020a). A measurement methodology with a very short response time and high accuracy is chosen for the determination of the maximum temperatures. A simple, yet highly precise solution is to use temperature indicating lacquers. Temperature indicating lacquers have an accuracy of  $\pm 1.0\%$  and a very short response time of 1 ms (OMEGA Engineering 2004) and are therefore superior to alternative measuring methods such as thermography or thermocouples (Roth et al., 2020a). Since the lacquers are applied in a very thin layer, it is assumed that the temperature of the lacquers is identical to the metal surface. Temperature differences due to conduction are neglected.

For measurement, the temperature indicating lacquers are applied in a thin layer to the areas to be examined with repetitive accuracy by using a stencil (see Fig. 5) (Roth et al., 2020a). Each temperature lacquer is designed for a defined temperature and melts when reaching it (OMEGA Engineering 2004). The melting leads to a visible change because the lacquer changes its opaque colour and appears shiny transparent after the temperature shift, as shown in Fig. 6. A total of four different temperature indicating lacquers with temperature increments of 149 °C,

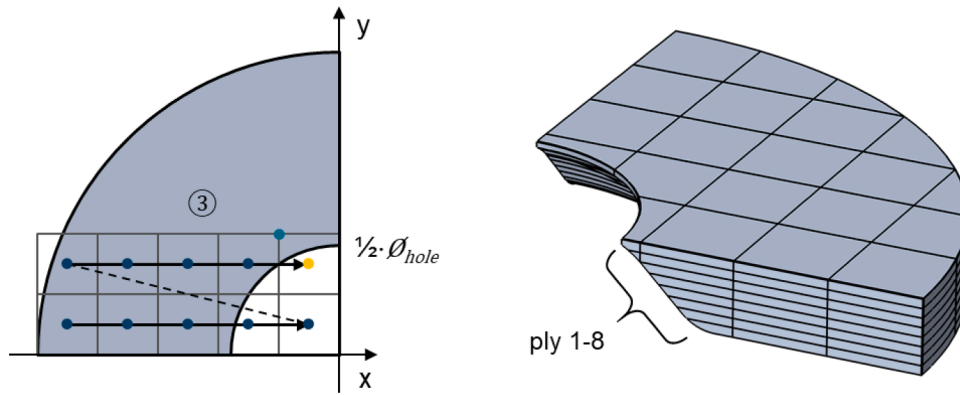


Fig. 3. Discretization of the material parameters.

**Table 2**  
Specific temperature-dependant material parameters.

Temperature [°C]	Steel DC04 (Richter, 2020)*Measured			Copper alloy CuCrZ1 (Deutsches Kupferinstitut 2021)		
	Specific electric conductivity [s] S/m	Specific heat capacity [J/(kg K)]	Specific thermal conductivity [W/(m K)]	Specific electric conductivity [s] S/m	Specific heat capacity [J/(kg K)]	Specific thermal conductivity [W/(m K)]
0	5.92	445.76*	46.67*	43	370	310
100	4.35	493.87*	51.63*	36	450	315
200	3.29	532.58*	53.87*	28	480	324
300	2.54	572.37*	50.84*	23	500	333
400	2.00	611.00	40.90	20	500	336
500	1.60	677.00	37.70			
600	1.30	778.00	34.5			
700	1.08	880.00	31.50			
900	0.95	1000.00	28.00			

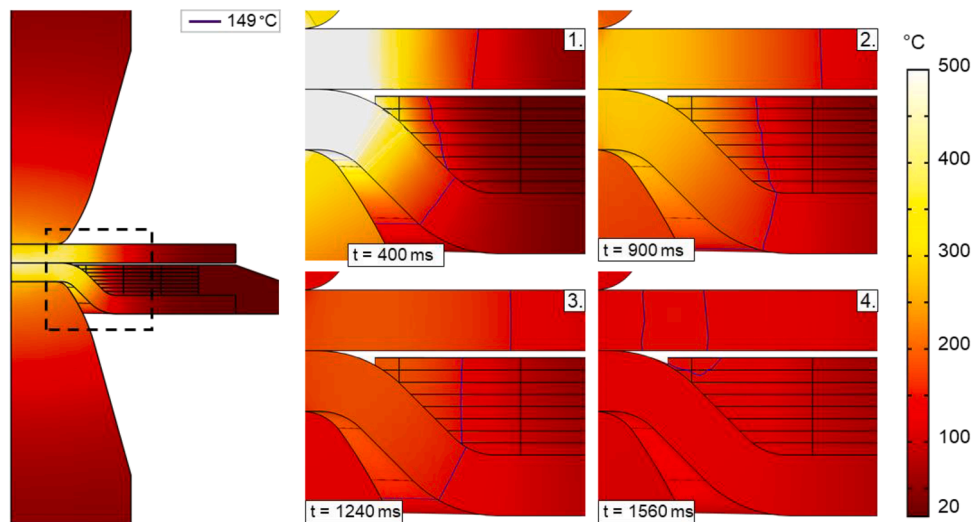


Fig. 4. Temporal and spatial distribution of temperature.

**Table 3**  
Results of the sensitivity analysis.

Isotherm	Radial distance of the isotherms in millimetres from the centre of the sample					
	Electric contact resistance			Electrical conductivity of DC04		
	-30%	normal	-30%	-30%	Standard	+30%
149 °C	6.58	7.06	7.40	7.88	7.06	6.60
253 °C	4.89	5.04	5.24	5.50	5.04	4.87
343 °C	4.32	4.46	4.62	4.78	4.46	4.33
454 °C	3.95	4.10	4.20	4.15	4.10	3.99

253 °C, 343 °C and 454 °C are used. By optically measuring the distance from the turnover point to the centre of the inserts, four local temperature maxima can thus be determined.

Fig. 7. shows the temperature differences between numerical model and experimental measurements on the basis of the four local maxima with the temperatures 149 °C, 253 °C, 343 °C and 454 °C. The distance to the centre of the weld spot or the centre of the insert can be read on the x-axis. For the insert geometry with a  $\varnothing_{hole}$  of 9.0 mm, it is shown that the numerical model has very good agreement with the experimental measured values. The deviations only amount to 6.38% and 2.51% for the temperatures 343 °C and 454 °C (see Table 4). For the

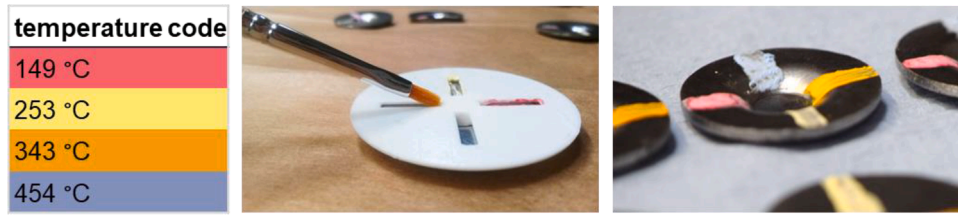


Fig. 5. Application of the four different temperature indicating lacquers to the metal inserts.

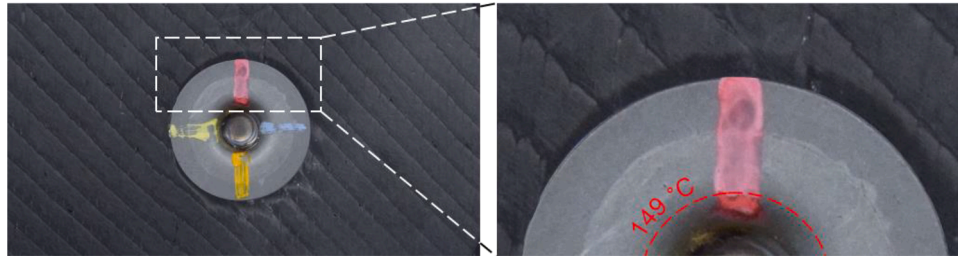


Fig. 6. Visual change of the temperature indicating lacquers by melting at application temperature.

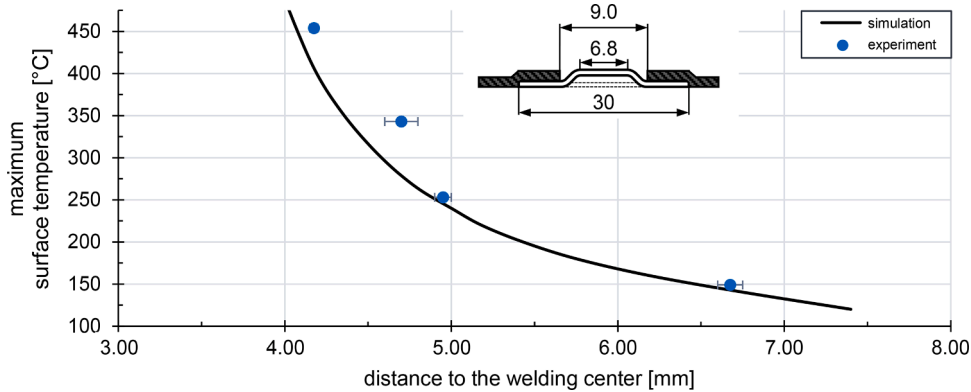


Fig. 7. Comparison of the local temperature maxima between model and measurements for a hole diameter  $\phi_{hole}$  of 9.0 mm.

Table 4

Deviations between numerical results and measured values for the four control temperatures.

$\phi_{hole}$	149 °C	253 °C	343 °C	454 °C
9 mm	0.37%	0.10%	6.38%	2.51%
14 mm	0.88%	0.80%	5.70%	2.06%
16 mm	1.60%	0.39%	6.65%	2.33%

comparative temperatures of 149 °C and 253 °C, there are only deviations of 0.37% or 0.10%. These temperatures are more critical because from the temperature range above 200 °C onwards, damage to the matrix occurs.

The deviations at 343 °C and 454 °C of 6.38% and 2.51% in the direct vicinity of the welding lens can be explained by the fact that a slight thinning of the material occurs due to the cold forming during the production of the insert. This material thinning causes a negative, local change in thermal conductivity, which is not considered in the numerical model. The deviations for other hole diameters  $\phi_{hole}$  also show the high accuracy of the numerical model (see Table 4).

A closer look at the results shows that the local temperature in the CFRP with a hole diameter  $\phi_{hole}$  of 9.0 mm and a distance to the welding centre of 4.5 mm is about 300 °C (see Fig. 7). At such a high temperature, the thermoset matrix is exposed to damage and degradation occurs (Visakh and Visakh, 2015; Natarajan and Murugavel, 2017). Therefore,

the hole diameter  $\phi_{hole}$  must be enlarged for damage-free welding. Fig. 8 exemplarily shows the iterative determination of the minimum hole diameter required for welding without damage. Temperatures up to 220 °C can be regarded as damage-free for the considered application and the used matrix system. It can be seen that no more damage occurs for the selected configuration with a hole diameter of 11.3 mm and above.

For practical application, a safety factor of at least 1 mm is recommended in order to maintain sufficient tolerance against possible damage stemming from minor deviations during production or the imprecise positioning of the welding tongs with the robot.

**Conclusion**

Numerical and experimental investigations were carried out to study the resistance spot welding of shell-shaped FRP components with a metallic insert in terms of temperature distribution. The aim was to realise damage-free resistance spot welding for joining FRP/metal components by developing a precise process understanding.

A numerical model that precisely maps the path of the fibres and thus the anisotropic properties was built for this purpose. In addition, all material properties that influence the temperature distribution are implemented in the model. The model can be parameterised, allowing different geometries and layer structures to be calculated for individualised welding tasks. The respective temperature maxima in the area of

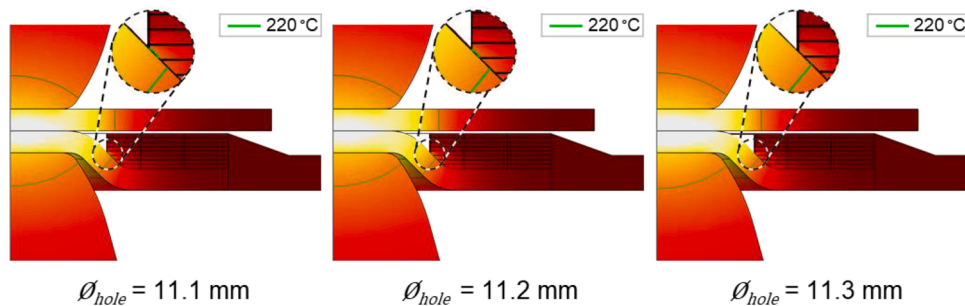


Fig. 8. Iterative determination of the minimum hole diameter  $\varnothing_{hole}$  for the inserts.

the insert and the FRP are obtained as a result. It turns out that the orientation of the fibres and the diameter of the insert have negligible influences on the temperature maxima. In contrast, the energy input during welding and the CFRP hole diameter significantly influence the resulting temperature maxima and thus the potential damage to the laminate. It is therefore appropriate to design the CFRP hole diameter sufficiently large to exclude degradation of the laminate's thermoset matrix. Experimental investigations with temperature indicating lacquers confirm the results of the numerical model and show a high prediction quality with only minor deviations between measured and calculated temperature maxima.

The results of the research demonstrate that damage-free resistance spot welding of FRP/metal components can be realised when the degradation temperature of the matrix is taken into account. This creates new opportunities for integrating FRP components into a metallic base structure. In addition to conventional bonding, riveting, bolting and screwing, cost-efficient and highly automatable resistance spot welding may also be considered as a potential process for joining FRP components in the future.

#### Declaration of competing interest

The authors declare that they have no known competing financial interests or personal relationships that could have appeared to influence the work reported in this paper

#### Acknowledgements

This work was supported by the German Research Foundation (DFG: Deutsche Forschungsgemeinschaft, Project No.: 418238897).

#### References

- Akkus, A., 2009. Temperature distribution study in resistance spot welding. *J. Sci. Ind. Res.* 68.
- Bardon, J.P., Tahar, L., 2001. Estimation of thermal contact conductance during resistance spot welding. *Exp. Heat Transf.* 14 (4), 251–264. <https://doi.org/10.1080/089161501317098308>.
- Boutaris, K., Kirbach, M., Becker, W., 2011. Faserverbundwerkstoff-Bauteil mit Metallischem Anschlussstück und Damit Gefertigtes Verbundbauteil (DE 10 2011 116 300 B4).
- Cho H.S., Cho Y.J. Study of the thermal behavior in resistance spot welds 1989;68: 236s–244s.
- Deutsches Kupferinstitut. Datenblatt CuCr1Zr. [June 15, 2021]; Available from: [https://www.kupferinstitut.de/fileadmin/user\\_upload/kupferinstitut.de/de/Documents/Shop/Verlag/Downloads/Werkstoffe/Datenblaetter/Niedriglegierte/CuCr1Zr.pdf](https://www.kupferinstitut.de/fileadmin/user_upload/kupferinstitut.de/de/Documents/Shop/Verlag/Downloads/Werkstoffe/Datenblaetter/Niedriglegierte/CuCr1Zr.pdf).
- Dominginghaus, H., Elsner, P., Eyerer, P., Kunststoffe, H.T., 2012. Eigenschaften Und Anwendungen, 8th ed. Springer, Berlin, Heidelberg.
- Fleischer, J., Teti, R., Lanza, G., Mativenga, P., Möhring, H.-C., Caggiano, A., 2018. Composite materials parts manufacturing. *CIRP Ann.* 67 (2), 603–626.
- Friedrich, H.E., 2017. Leichtbau in Der Fahrzeugtechnik, 2nd ed. Springer Vieweg, Wiesbaden.
- Gebhardt, J., Schwennen, J., Lorenz, F., Fleischer, J., 2018. Structure optimisation of metallic load introduction elements embedded in CFRP. *Prod. Eng.* 12 (2), 131–140. <https://doi.org/10.1007/s11740-018-0820-5>.

- Ghasemi Nejjhad, M.N., Chou, T.-W., 1990. A model for the prediction of compressive strength reduction of composite laminates with molded-in holes. *J. Compos. Mater.* 24 (3), 236–255. <https://doi.org/10.1177/002199839002400301>.
- Gibbins, J., 2006. Thermal Contact Resistance of Polymer Interfaces [Mastertheses]. Waterloo: University of Waterloo.
- Han, Z., Orozco, J., Indacochea, J.E., Chen, C.H., 1989. Resistance spot welding: a heat transfer study: real and simulated welds were used to develop a model for predicting temperature distribution. *WRC* 343, 363–371.
- Hartmann, S., Kheiri Marghzar, A., 2018. Modeling of fiber circumplacement around a hole using a streamline approach. *Univ. J. Math. Appl.* 1 (1), 17–28. <https://doi.org/10.32323/ujma.398481>.
- Hartmann, S., Kheiri Marghzar, A., Gilbert, R.R., Pangboonyanon, W., Meiners, D., 2020. Experiment and simulation of bypassing holes in composites. *Compos. Struct.* 234, 111666 <https://doi.org/10.1016/j.compstruct.2019.111666>.
- Hufenbach, W., G. R., Kupfer, R., 2011. Bolted joints with moulded holes for textile thermoplastic composites. In: ICCM International Conferences on Composite Materials.
- Kunze, A., Jansen, F., von Hehl, A., 2016. Numerical Simulation of weldable metallic force transmission points in fibre reinforced thermoplastics (FRTP). In: Proceedings of the 17th European Conference on Composite Materials: ECCM17 - 17th European Conference on Composite Materials, 26-30th June 2016. Munich, Germany.
- Augsburg. MAI Carbon Cluster Management GmbH, pp. 1–6.
- Kupfer, R., 2016. Zur Warmlochformung in Textil-Thermoplast-Strukturen Technologie, Phänomenologie, Modellierung [Dissertation]. Technische Universität Dresden, Dresden.
- Lee, Y., Jeong, H., Park, K., Kim, Y., Cho, J., 2017. Development of numerical analysis model for resistance spot welding of automotive steel. *J. Mech. Sci. Technol.* 31 (7), 3455–3464. <https://doi.org/10.1007/s12206-017-0634-y>.
- Leiser, J., 2006. Beitrag zu innovativen Verbindungstechniken für Hochleistungsverbundwerkstoffe. Zugl.: chemnitz, Techn. Univ., Diss., 2006. Chemnitz: Inst. für Allg. Maschinenbau und Kunststofftechnik.
- Lin, H.J., Lee, Y.J., 1992. Strength of composite laminates with continuous fiber around a circular hole. *Compos Struct.* 21 (3), 155–162.
- Lin, H.J., Tsai, C.C., Shie, J.S., 1995. Failure analysis of woven-fabric composites with moulded-in holes. *Compos. Sci. Technol.* 55 (3), 231–239.
- Lin, H.J., Yang, S.H., 1993. Modeling and Analysis of Composite Laminates with Continuous Fiber around a Circular Hole. *J. Compos. Mater.* 27 (5), 513–525. <https://doi.org/10.1177/002199839302700504>.
- Lu, Y., Peer, A., Abke, T., Kimchi, M., Zhang, W., 2018. Subcritical heat affected zone softening in hot-stamped boron steel during resistance spot welding. *Mater. Des.* 155, 170–184. <https://doi.org/10.1016/j.matdes.2018.05.067>.
- Natarajan, M., Murugavel, S.C., 2017. Thermal stability and thermal degradation kinetics of bio-based epoxy resins derived from cardanol by thermogravimetric analysis. *Polym. Bull.* 74 (8), 3319–3340.
- Ng, S.-P., Tse, P.-C., Lau, K.-J., 2001. Progressive failure analysis of 2/2 twill weave fabric composites with moulded-in circular hole. *Compos. Part B* 32 (2), 139–152. [https://doi.org/10.1016/S1359-8368\(00\)00040-8](https://doi.org/10.1016/S1359-8368(00)00040-8).
- Nied, H., 1984. The finite element modeling of the resistance spot welding process. *Weld. J.* 63 (4), 123-s-132-s.
- Njuguna, J., 2016. Lightweight Composite Structures in Transport: Design, Manufacturing, Analysis and Performance. s.l. Elsevier Science.
- OMEGA Engineering, 2004. Datenblatt OMEGALAQ und TAP. OMEGALAQ™ Temperaturmesslack TAP Thermolement-Aufklebepads, Deckenpfornn. Available from: <https://www.omega.de/temperature/pdf/LAQ.pdf>.
- Pilling, M.W., Yates, B., Black, M.A., 1979. The thermal conductivity of carbon fibre-reinforced composites. *J. Mater. Sci.* (14), 1326–1338.
- Pischinger, S., Seiffert, U., 2016. Vieweg Handbuch Kraftfahrzeugtechnik, 8th ed.
- Radaj, D., 1988. Wärmewirkungen Des Schweißens: Temperaturfeld, Eigenspannungen. Springer Berlin Heidelberg, Verlag. Berlin, Heidelberg.
- Reuss, A., 1929. Berechnung der fließgrenze von mischkristallen auf grund der plastizitätsbedingung für einkristalle. *Z. Angew. Math. Mech.* 9 (1), 49–58. <https://doi.org/10.1002/zamm.19290090104>.
- Richter F.. The Physical Properties of Steels Part 1: tables and Figures; Available from: [https://www.tugraz.at/fileadmin/user\\_upload/Institute/IEP/Thermophysics\\_Group/Files/Staeble-Richter.pdf](https://www.tugraz.at/fileadmin/user_upload/Institute/IEP/Thermophysics_Group/Files/Staeble-Richter.pdf).
- Roquette, D., Meyer, F., Herbeck, L., 2017. High Volume Manufacturing of Carbon Fiber Reinforced Plastics for Body in White. *Materialien des Karosseriebaus* 2017. Bad Nauheim 16, 18.05.

- Roth, S., Pracisnore, F., Coutandin, S., Fleischer, J., 2020a. A new approach for modelling the fibre path in bolted joints of continuous fibre reinforced composites. *Compos. Struct.* 243, 112184 <https://doi.org/10.1016/j.compstruct.2020.112184>.
- Roth, S., Hezler, A., Pampus, O., Coutandin, S., Fleischer, J., 2020c. Influence of the process parameter of resistance spot welding and the geometry of weldable load introducing elements for FRP/metal joints on the heat input. *J. Adv. Joining Process.* 2, 100032 <https://doi.org/10.1016/j.jajp.2020.100032>.
- Roth, S., Warneck, M., Coutandin, S., Fleischer, J., 2019. RTM Process manufacturing of spot-weldable CFRP-metal components. *Lightw. Des. Worldwide* 12 (5), 18–23. <https://doi.org/10.1007/s41777-019-0046-z>.
- Ruffing, T., Baron, S., 2019. *Inserts For In-Situ Integration of Assembly Interfaces Into Composite Materials*. ARaymond Center of Expertise, Saint Louis, France. Detroit.
- Sika Deutschland GH. Biresin CR170-CH170-3 Composite Resin System. [June 15, 2021]. Available from: <https://industry.sika.com/dms/getdocument.get/b41b1a25-8ac1-497f-bf79-f2e5a8a3747b/Biresin-CR170-CH170-3-New.pdf>.
- SIKA Dr. Siebert & Kuhn GmbH & Co.KG, 2020. Table of Emissivity. Available from: [https://www.sika.net/images/Documents/Table\\_of\\_Emissivity.pdf](https://www.sika.net/images/Documents/Table_of_Emissivity.pdf).
- Toray Composite Materials America, Inc. T700S, 2020. Standard Modulus Carbon Fiber.
- Visakh, PM (Ed.), 2015. *Thermal Degradation of Polymer Blends, Composites and Nanocomposites*. Springer International Publishing, Cham, s.l.
- Voigt, W., 1889. Ueber die Beziehung zwischen den beiden Elasticitätsconstanten isotroper Körper. *Ann. Phys.* 274 (12), 573–587. <https://doi.org/10.1002/andp.18892741206>.
- von Hehl, A., Kunze, A., Jansen, F., Meyer, M., 2016. Structural design of spot weldable force transmission elements for FRTP automotive panels. *Materials in Car Body Engineering 2016*. Automotive Circle International, Bad Nauheim. Vincentz Network.
- Wan, X., Wang, Y., Zhang, P., 2014b. Modelling the effect of welding current on resistance spot welding of DP600 steel. *J. Mater. Process. Technol.* 214 (11), 2723–2729. <https://doi.org/10.1016/j.jmatprotec.2014.06.009>.
- Wan, X., Wang, Y., Zhang, P., 2014a. Modelling the effect of welding current on resistance spot welding of DP600 steel. *J. Mater. Process. Technol.* 214 (11), 2723–2729. <https://doi.org/10.1016/j.jmatprotec.2014.06.009>.
- Wang, J., Wang, H.-P., Lu, F., Carlson, B.E., Sigler, D.R., 2015. Analysis of Al-steel resistance spot welding process by developing a fully coupled multi-physics simulation model. *Int. J. Heat Mass Transf.* 89, 1061–1072. <https://doi.org/10.1016/j.ijheatmasstransfer.2015.05.086>.
- Weatherhead, R.G., 1980. *FRP Technology: Fibre Reinforced Resin Systems*. Springer, Dordrecht/Netherlands.
- Zhao, D., Wang, Y., Zhang, P., Liang, D., 2019. Modeling and experimental research on resistance spot welded joints for dual-phase steel. *Materials (Basel)* 12 (7). <https://doi.org/10.3390/ma12071108>.